



Self-assembled mesoporous TiO₂/carbon nanotube composite with a three-dimensional conducting nanonetwork as a high-rate anode material for lithium-ion battery

Jie Wang^{a,b}, Ran Ran^{a,b}, Moses O. Tade^d, Zongping Shao^{a,c,d,*}

^a State Key Laboratory of Materials-Oriented Chemical Engineering, Nanjing University of Technology, No. 5 Xin Mofan Road, Nanjing 210009, China

^b College of Chemistry & Chemical Engineering, Nanjing University of Technology, No. 5 Xin Mofan Road, Nanjing 210009, China

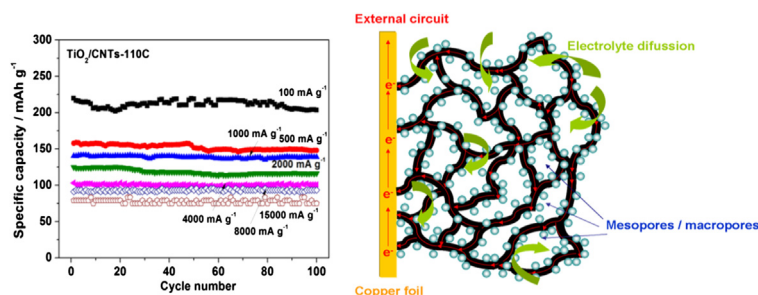
^c College of Energy, Nanjing University of Technology, No. 5 Xin Mofan Road, Nanjing 210009, China

^d Department of Chemical Engineering, Curtin University, Perth, WA 6458, Australia

HIGHLIGHTS

- TiO₂/CNT hybrids were prepared by a facile PEO-aided self-assembled process.
- CNTs in the TiO₂/CNT hybrids construct a 3D conductive network.
- PEO plays an important role on the TiO₂ well dispersion in the TiO₂/CNT hybrids.
- TiO₂/CNTs-110 C hybrids showed a high electronic conductivity (5.13 S cm⁻¹).
- TiO₂/CNTs-110 C anodes revealed excellent rate and good cycling performance.

GRAPHICAL ABSTRACT



ARTICLE INFO

Article history:

Received 27 October 2013

Received in revised form

2 December 2013

Accepted 19 December 2013

Available online 31 December 2013

Keywords:

Lithium ion batteries

Titanium dioxide/carbon nanotube hybrids

Self-assemble

High-rate anodes

ABSTRACT

Mesoporous three-dimensional (3D) TiO₂/carbon nanotube conductive hybrid nanostructures can be successfully developed using polyethylene oxide (PEO) to modify the surfaces of carbon nanotubes (CNTs). During the synthesis process, PEO acts as not only “bridges” to connect the TiO₂ nanoparticles to the CNT surfaces but also as “hosts” to accommodate and stabilize the in situ generated TiO₂ particles. As the electrodes for lithium-ion batteries, such mesoporous 3D TiO₂/CNT hybrids, demonstrate high Li storage capacity, superior rate performance and excellent long-term cycling stability. They exhibit a reversible specific capacity of 203 mA h g⁻¹ at 100 mA g⁻¹ and a stable capacity retention of 91 mA h g⁻¹ at 8000 mA g⁻¹ (47.6 C) over 100 cycles; they also retain approximately 90% (71 mA h g⁻¹) of their initial discharge capacity after 900 cycles at an extremely high rate of 15,000 mA g⁻¹ (89 C). This facile synthetic strategy to construct mesoporous 3D TiO₂/CNT conductive hybrids provides a convenient route that efficiently assembles various inorganic oxide components on the CNTs’ surfaces and enables the formation of heterogeneous nanostructures with novel functionalities. In particular, utilizing a conductive 3D CNT network can serve as a promising strategy for developing high-performance electrodes for Li secondary batteries and supercapacitors.

© 2014 Elsevier B.V. All rights reserved.

* Corresponding author. College of Energy, Nanjing University of Technology, No. 5 Xin Mofan Road, Nanjing 210009, China. Tel.: +86 25 83172256; fax: +86 25 83172242.

E-mail address: shaozp@njut.edu.cn (Z. Shao).

1. Introduction

As one of the most well developed electrochemical energy storage devices, lithium-ion batteries (LIBs) are highly promising power sources for electric and hybrid electric vehicles (EVs and HEVs), because of their high energy density, no memory effect and long cycle life. However, the power density is typically low in state-of-the-art LIBs utilizing LiCoO_2 cathodes and graphite anodes; this factor is mainly limited mainly by slow Li-ion diffusion, poor electron transport in the electrodes and large resistance values at the interface of electrode/electrolyte interface [1,2]. For large-scale applications, safety is also a major concern, and the carbon/graphite electrodes remain problematic due to prohibitively low lithium intercalation potentials (~ 0.1 V). Some oxides and composite oxides, such as TiO_2 and $\text{Li}_4\text{Ti}_5\text{O}_{12}$, are promising alternative materials for anodes because they display favorable theoretical capacities and greatly improved safety profiles due to their higher lithium intercalation potentials. To achieve high power density and develop new electrode materials, it is important to explore new electrode architectures that can provide interconnected nanopaths for electrolyte-ion transport and electronic conduction, thus effectively reducing polarization of electrode under high charge/discharge rates [3]. Currently, various approaches have been developed to enhance electron transport in electrode materials, such as incorporating matrices or conductive additives (metals [4], metal oxides [5–7] and carbonaceous materials [8–11]), and to improve the lithium-ion diffusivity inside electrode material through the construction of electrode nanostructures, for example, nanowires [12], nanotubes [13], core/shell nanocomposites [14] and 3D mesoporous structures [15].

Some 3D mesoporous materials are attractive hosts for lithium storage because of their large surface area, ensuring high contact area between the electrolyte and electrode, thin walls, providing short Li-ion diffusion distance in the solid phase, and rich pores, allowing the easy wetting of hollow spaces by the liquid electrolyte, and facilitating electrolyte ions transport inside the electrode materials and giving good accommodation of strain during rapid charge/discharge processes [15,16]. However, carbonaceous materials have grown more popular as conductive additives structures, such as two-dimensional (2D) graphene and one-dimensional (1D) CNTs, have been studied for their superior electronic conductivity, high surface-to-volume ratio, ultrathin walls, structural flexibility, large specific area and chemical stability [17,18]. Specifically, the electronic conductivity of CNTs at room temperature approaches $5 \times 10^5 \text{ S m}^{-1}$, and their length-to-diameter ratio exceeds 10,000, revealing a much lower conduction threshold than other carbon conductive additives. Notably, 1D CNTs can be well connected to the others by π – π interactions with the formation of 3D conductive networks in a more efficient way than graphene conductive additives, providing continuous conductive pathways for electron transport [19]. By constructing mesoporous 3D hybrid nanostructures that incorporate 3D CNT conductive networks, rapid electron transfer and lithium ion transport in the electrode materials can be realized, especially at high charge/discharge rates. Moreover, the 3D CNTs also facilitate the dispersion of nanoparticles because of their large surface area. Therefore, improved electrode performance may be achieved by applying these unique electrode architectures, particularly at rapid rates.

Anatase TiO_2 is a promising anode material for lithium ion batteries because it exhibits a high capacity and chemical stability. However, using TiO_2 materials in Li-ion batteries remains limited because of relatively slow Li-ion diffusion and poor electron transport within the electrodes, leading to rather poor cycling performance of TiO_2 electrodes [20]. Mesoporous 3D conductive network hybrid nanostructures containing CNTs and anatase TiO_2

feature CNT distributions that provide continuous electronic paths, similar to blood vessels in the human body, and subsequently ensure rapid electron transfer. When synthesizing mesoporous TiO_2/CNT 3D conductive network hybrid nanostructures, the graphitic surface of CNT tends to be chemically inert and shows poor solubility; therefore, activating this surface is critical [21]. Covalently functionalizing CNTs via ultrasonication in strong acid circumvents this issue, allowing CNT-based composite fabrication. However, this process inevitably destroys the CNT band structures and shortens the CNTs, compromising the electronic and mechanical properties. Furthermore, the TiO_2 coatings installed on CNTs tend to be highly nonuniform [19,22,23]. Consequently, reliable syntheses of CNT-based heterogeneous nanohybrids using non-covalent approaches have become a research focus [19,22,23].

In this study, we present a new route that applies a uniform TiO_2 coating onto pristine CNTs without covalent functionalization; this process is achieved using PEO to modify the CNT surfaces in a solution-based synthesis process, and the PEO is easily removed under low-temperature thermal treatment in air. PEO serves two purposes: it helps disperse the CNTs in solution by adhering onto their surfaces via physical absorption and/or weak covalent bonding and acts as a bridge, integrating the TiO_2 onto the CNT surfaces. Subsequently, the modified CNTs can be joined with TiO_2 nanoparticles, yielding 3D TiO_2/CNT hybrid conductive networks after a thermal treatment (Scheme 1); these material exhibit tailored properties while retaining the high electronic conductivity of the CNTs. We report that using the mesoporous TiO_2/CNT 3D conductive network hybrids as anodes for lithium ion batteries cause a significant increase in the discharge capacity at high rates and excellent long term cycling stability relative to mesoporous TiO_2 and other TiO_2/CNT composites [14,23–26].

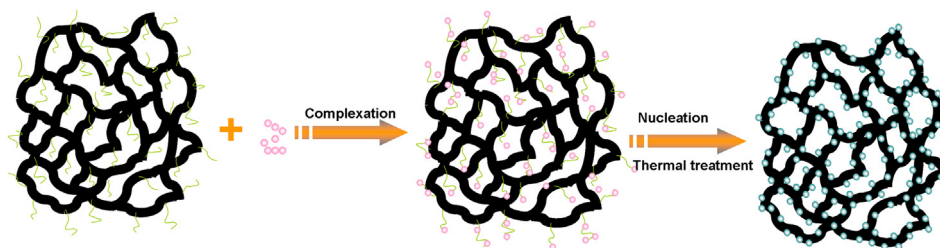
2. Experimental

2.1. Fabrication of mesoporous TiO_2 and 3D conductive network TiO_2/CNT hybrids

All reagents were of analytical grade and used as received without further purification. The average outer diameter of the multi-walled carbon nanotubes (MWCNTs) was 30–50 nm, and the average length was between 10 and 20 μm . In a typical experiment, 0.02 g of PEO (M n: 600,000) was dissolved in 60 ml of an ethanol/water solution (2:1 v/v); subsequently, 0.1 g of CNTs was dispersed in the PEO ethanol/water solution via ultrasonication for 10 min. Moreover, 1 ml of tetrabutyl titanate $\text{Ti}(\text{O}i\text{Bu})_4$ was added to 50 ml of acetic acid/ethanol (1:4 v/v). The PEO–CNT dispersions and the tetrabutyl titanate solution were mixed via stirring at 60 °C for 22 h. Subsequently, the products were washed repeatedly with water and ethanol several times using centrifugation before drying in a 60 °C oven for 24 h in air. Finally, the powder and the PEO–CNT precipitate were ground and annealed at 400 °C for 2 h in air to generate TiO_2/CNTs -60 C and CNTs (PEO), respectively. Mesoporous TiO_2 was prepared for comparison using the same synthesis route as the TiO_2/CNTs -60 C and omitting the CNTs. Similarly, a TiO_2/CNT sample without PEO was also synthesized at 60 °C and labeled TiO_2/CNTs -60 C (without PEO). A sample was generated using the same method as for the TiO_2/CNTs -60 C sample except that the reaction temperature was adjusted to go up to 110 °C from room temperature and then immediately cool down to 60 °C with a rate of 10 °C min^{-1} ; this material was denoted TiO_2/CNTs -110 C.

2.2. Structural and morphological characterization

The crystal structures of the samples were characterized via X-ray diffraction (XRD) using a Bruker D8 Advance diffractometer



Scheme 1. PEO mediated formation and stabilization of 3D CNT conductive network and growth of self-assembled TiO_2/CNT hybrids.

with filtered Cu $K\alpha$ radiation. The diffraction patterns were collected at room temperature by step scanning in the $10^\circ \leq 2\theta \leq 90^\circ$ range. The morphologies and microstructures of the products were investigated using field emission scanning electron microscopy (FE-SEM, Hitachi S-4800) and transmission electron microscopy (TEM, JEOL JEM-200CX). Raman spectra were recorded

using a Horiba HR 800 with an argon ion laser operating at 514 nm for excitation. X-ray photoelectron spectroscopy (XPS) measurements and analysis were conducted using a PHI 550 System. The specific surface area was determined using the N_2 adsorption at liquid nitrogen temperatures with a BELSORP II instrument. Before analysis, the samples were treated at 150°C for 2 h under vacuum to remove any surface-adsorbed species. The surface area was calculated using the Brunauer–Emmett–Teller (BET) equation. The pore-size distributions were calculated using the Barrett–Joyner–Halenda (BJH) method with the adsorption branch of the isotherm. Thermogravimetric analysis (TGA) and differential scanning calorimetry (DSC) were performed on an STA-409 PC TG thermal analyzer (NETZSCH-Gerätebau, Germany), with a heating rate of $10^\circ\text{C min}^{-1}$ from room temperature to 800°C .

2.3. Electrochemical measurements

The mesoporous TiO_2 and TiO_2/CNT hybrids annealed at 400°C for 2 h in air (TiO_2/CNTs -60 C and TiO_2/CNTs -110 C) were used as electrodes during the electrochemical measurements. The test cells were configured as Li metal (–)|electrolyte|mesoporous TiO_2 or TiO_2/CNT hybrids (+) with a liquid electrolyte (1 M solution of LiPF_6 in 1:1 ethylene carbonate (EC)–dimethyl carbonate (DMC)). Microporous polypropylene film (Celgard 2400) was used as the cell separator. The working electrode was prepared from a paste containing 85 wt.% active materials with 10 wt.% conductive Super P (conductive carbon black, NCM HERSBIT Chemical Co. Ltd., China) and 5 wt.% PVDF (polyvinylidene fluoride, Aldrich) in NMP (N-methyl-2-pyrrolidone). The slurries were deposited onto copper foil current collectors ($10\ \mu\text{m}$) with a scalpel; the current collectors were pretreated by etching with 1 M nitric acid solutions followed by rinsing with water and acetone. Before the electrochemical evaluation, the electrodes were dried under vacuum at 100°C for 24 h. The cells were assembled in an Ar-filled glove box. The cell was charged and discharged between 1.0 and 3.0 V at different current rates using a NEWARE BTS-5V50 mA computer-controlled battery test station. Cyclic voltammetry was performed from 1.0 to 3.0 V at 0.1, 0.5, 1, 2 and $4\ \text{mV s}^{-1}$ using a Princeton Applied Research (PARSTAT 2273) advanced electrochemical system. All of the electrochemical experiments were conducted at 25°C . The complex impedance measurements were also performed using a Princeton 2273 electrochemical system with single cells at open circuit voltages from 100 kHz to 5 mHz. A perturbation of 10 mV was applied, and the data were collected using a PC.

3. Results and discussion

3.1. Construction of 3D conductive network TiO_2/CNT hybrids

To construct the 3D CNT conducting networks, the CNTs must be well dispersed in liquid. Because the pristine CNTs are hydrophobic, CNTs precipitate from water easily; however, they may be

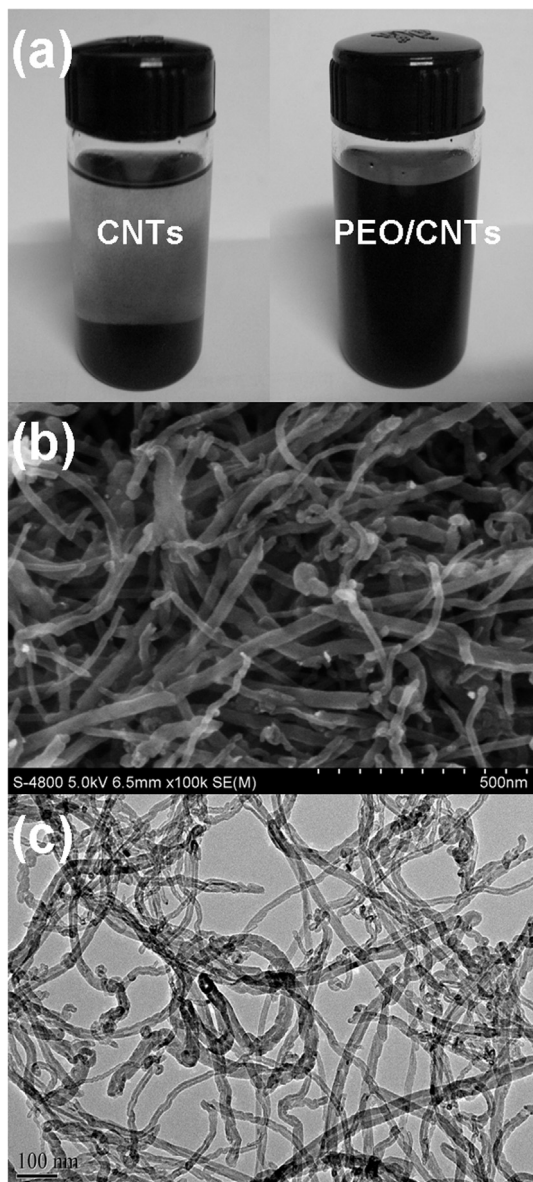


Fig. 1. Photographs of pristine CNTs and PEO/CNTs sols in water/ethanol solution (a), FE-SEM image (b) and TEM image (c) of the CNTs (PEO) sample.

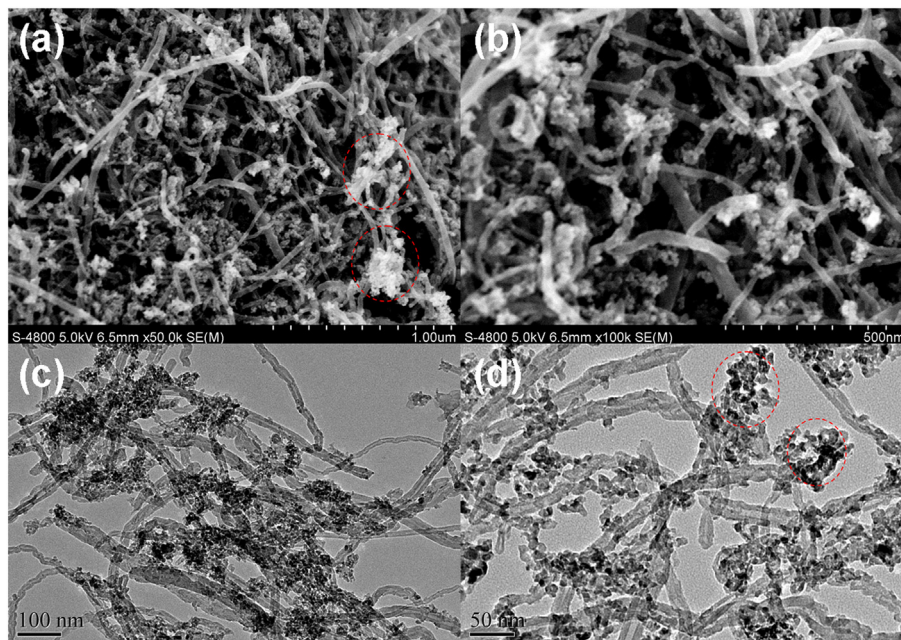


Fig. 2. FE-SEM (a) and TEM (c) images of the TiO_2/CNTs -60 C sample; (b) and (d) were magnified portions of (a) and (c), respectively.

distributed homogeneously in water via ultrasonication. Fig. 1a displays digital photographs of the CNTs dispersed in aqueous ethanol and the ink-like PEO/CNT sols after aging at ambient conditions for a couple of days. Without adding the PEO, the CNTs precipitated from the water/ethanol solution; the ink-like PEO/CNT sol remained stable. PEO contains numerous polyether segments and terminal hydroxyl groups that may physically adsorb and/or form weak covalent bonds with the few oxygen-containing functional groups on the surface of the pristine CNTs; the hydrogen bonding interactions between the PEO and H_2O molecules help stabilize the PEO/CNTs sols' formation. Because PEO contains numerous electron-rich oxygen atoms that can trap the Ti precursor on the modified CNT surfaces, this process is critical for forming the 3D TiO_2/CNT hybrid networks and will be discussed in detail later. As an insulator, the PEO contained in the 3D TiO_2/CNT hybrids might decrease the electronic conductivity; therefore, a 400 °C thermal treatment step was enacted for 2 h in air to remove the PEO. Fig. 1b and c presents the FE-SEM and TEM images of the CNT (PEO) samples after calcination. No impurity (e.g. amorphous carbon) remained on the CNTs surfaces, indicating that the PEO as surface modifier and organic materials of the reaction solution in the synthesis process were completely removed after the thermal treatment. Moreover, no residue could be found from the pristine PEO calcinated at 400 °C for 2 h in air. Therefore, we concluded that only the carbonaceous material formed from the heat treating of CNT remained in 3D TiO_2/CNT hybrids after the same post thermal treatment in air. In addition, the nanotube morphology survived this moderate thermal process, suggesting that the low-temperature calcinations in air did not extensively oxidize the CNTs; the morphology's survival was confirmed using the characteristic diffraction peaks of the CNTs in the XRD patterns collected after the calcinations (Fig. S1). As shown in Fig. 1c, the CNTs connected well with each other, forming a 3D network using the π - π interactions between CNTs.

By adding $\text{Ti}(\text{OBU})_4$ as the Ti precursor into the PEO/CNTs sols, the interaction between $\text{Ti}(\text{OBU})_4$ and PEO fixed the $\text{Ti}(\text{OBU})_4$ onto the CNT surfaces in ethanol/water. The $\text{Ti}(\text{OBU})_4$ hydrolyzed to form $\text{TiO}_2 \cdot x\text{H}_2\text{O}$ at a certain reaction temperature. After the subsequent

calcination at 400 °C, the $\text{TiO}_2 \cdot x\text{H}_2\text{O}$ was converted to TiO_2 and the PEO was eliminated simultaneously, forming a CNTs/TiO_2 hybrid with a 3D CNT network. Fig. 2 displays typical FE-SEM and TEM images of the CNTs/TiO_2 hybrid formed at 60 °C (initial reaction temperature); the PEO to CNTs to $\text{Ti}(\text{OBU})_4$ weight ratio was 1:5:50 (TiO_2/CNTs -60 C). The nanotubes survived the calcinations, becoming distributed across this hybrid material like blood vessels in the human body. When constructing the TiO_2/CNTs hybrids, the Ti precursor ($\text{Ti}(\text{OBU})_4$) was highly sensitive to water; the excess water derived from the PEO/CNT sols generally resulted in the significantly rapid hydrolysis reaction, forming particles instead of layer. The nucleation of TiO_2 particles occurred in a very short time followed by a growth process without super-saturation, generating a discontinuous coating; this result was confirmed using the FE-SEM and TEM images of 3D TiO_2/CNT hybrids prepared under various reaction temperatures, and the corresponding images are presented in Figs. 2 and 3. According to the FE-SEM images of the TiO_2/CNTs -60 C sample shown in Fig. 2a and b, the TiO_2 nanoparticles had agglomerated slightly, as marked by the red circles; however, they remained firmly attached to the CNT surfaces.

To validate the role of PEO during the development of the mesoporous 3D TiO_2/CNTs architecture, a synthesis of the CNT/TiO_2 hybrids was attempted without PEO, while all other synthetic parameters remained identical to those for TiO_2/CNTs -60 C; the resulting product was labeled TiO_2/CNTs -60 C (without PEO). In addition to the typical CNT (002) peaks, diffraction peaks attributed to the anatase TiO_2 phase also appeared in both the TiO_2/CNTs -60 C (without PEO) and TiO_2/CNTs -60 C samples in Fig. S1. Therefore, the PEO did not affect the phase evolution of the TiO_2/CNT hybrids. Fig. S3 displays the FE-SEM and TEM images for the TiO_2/CNTs -60 C (without PEO) sample. TiO_2 was revealed in the bulk materials' morphology, while few CNTs penetrated the TiO_2 bulk, demonstrating that the unfunctionalized CNTs had difficulty trapping the Ti precursor, while the PEO significantly affected the formation and dispersion of the TiO_2 particles. For comparison, mesoporous TiO_2 without CNTs was also prepared at 60 °C. The FE-SEM and TEM images in Fig. S2a and c revealed that the material existed mainly in bulk phase and displayed grains a few micrometers in size.

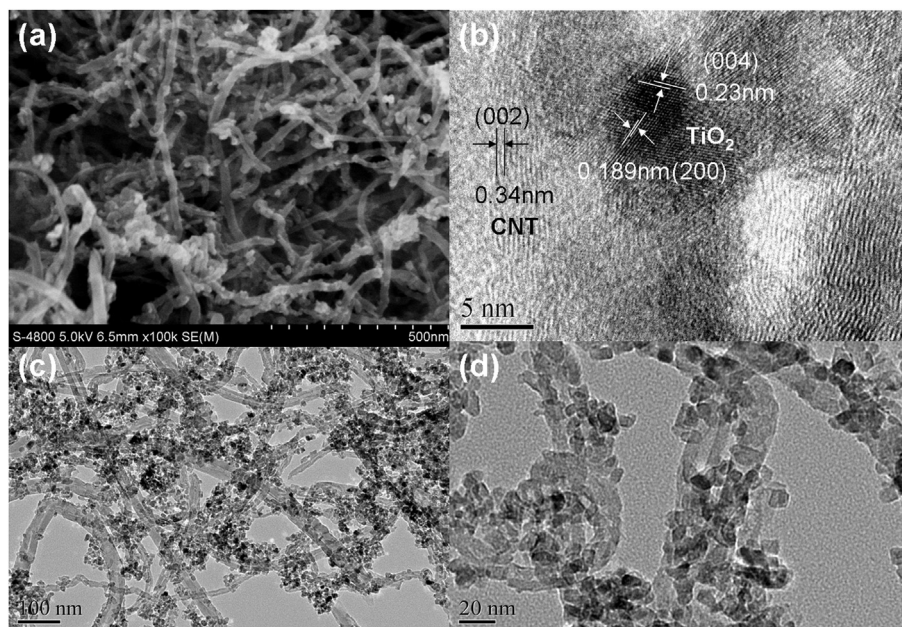


Fig. 3. FE-SEM image of the TiO₂/CNTs-110 C sample (a), TEM images of the TiO₂/CNTs-110 C sample: (b) high-resolution image clearly showing crystalline fringes, (c) low magnification image showing the well-dispersed TiO₂ nanoparticles on the CNTs surfaces, and (d) a magnified portion of (c).

According to the magnified images presented in Fig. S2b, the TiO₂ surface was relatively rough, while the bulk material was composed of many ultrafine nanoparticles ($\sim 2\text{--}3$ nm in size), leading to the highly porous structure presented in Fig. S2c and d. Consequently, the PEO was critical for forming the mesoporous 3D TiO₂/CNT architectures. Since the hydrolysis was closely related to the reaction temperature, a higher initial reaction temperature (110°C) was also utilized. Fig. 3 presents the FE-SEM and TEM images of the TiO₂/CNTs-110 C sample after calcination. No obvious TiO₂ agglomeration was observed in Fig. 3a for the TiO₂/CNTs-110 C sample, indicating that the TiO₂ nanoparticle coating was smoother relative to the TiO₂/CNTs-60 C sample. The high-resolution image of the TiO₂/CNTs-110 C sample in Fig. 3b revealed a fringe with a spacing of 0.34 nm, corresponding to the (002) crystalline plane of the multi-walled CNTs; in addition, lattice fringes with spacings of 0.23 and 0.189 nm were also visible, matching those of the (004) and (200) planes for anatase TiO₂, respectively. It suggested that the sample was composed of CNTs and anatase TiO₂, in well agreement with the XRD results. Moreover, the TEM image of the TiO₂/CNTs-110 C sample in Fig. 3c and d revealed that the TiO₂ particles grew to 8–10 nm, and whole 6–8 nm particles were observed in the TiO₂/CNTs-60 C sample (Fig. 2d); therefore, the initial reaction temperature exerted a significant effect on the TiO₂ particles' crystalline growth. Compared to the TiO₂ bulk material ($\sim 2\text{--}3$ nm in size) as shown in Fig. S2, a remarkable TiO₂ particle size increase appeared in the TiO₂/CNTs hybrids, this was because that PEO with enriched oxygen-containing groups adhering onto the CNTs trapped the Ti precursor quickly and speeded up the TiO₂ nucleation and growth, and simultaneously changed the TiO₂ particles dispersion. Additionally, the TiO₂ particles were well dispersed on the CNTs surfaces and distributed in this 3D TiO₂/CNT hybrids network with much less aggregation.

The TiO₂ nanoparticles' coverage of the 3D TiO₂/CNTs hybrid network for both the TiO₂/CNTs-60 C and TiO₂/CNTs-110 C samples was studied by measuring the weight loss (TGA) and heat flow (DSC) in air up to 800°C . Fig. 4 reveals that the TiO₂/CNTs-60 C and TiO₂/CNTs-110 C samples experienced weight losses of approximately 38.7 and 31.2 wt.%, respectively; these losses appeared

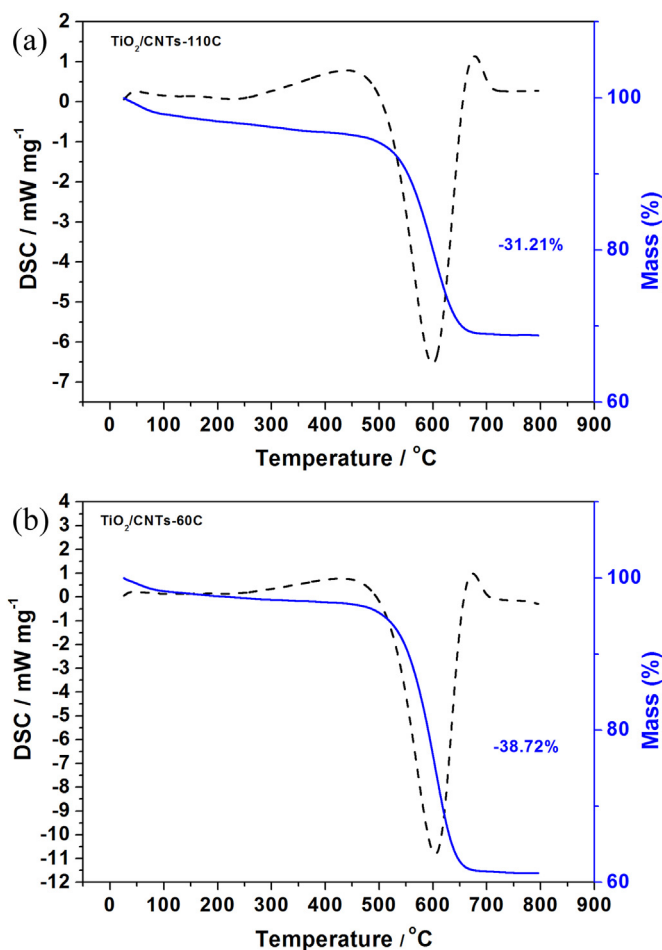


Fig. 4. The TGA (blue line) and DSC (black line) curves of the TiO₂/CNTs-110 C (a) and TiO₂/CNTs-60 C (b) samples. (For interpretation of the references to color in this figure legend, the reader is referred to the web version of this article.)

primarily between 470 and 670 °C in the TGA curve and were accompanied by a sharp exothermic peak in the DSC plots, which were attributed to the formation of gaseous CO₂ via CNT oxidation [22]. Only a little additional weight losses accompanied by a very broad exothermic peak in the DSC plots below 470 °C for the TiO₂/CNTs-60 C and TiO₂/CNTs-110 C samples were around 4 and 5 wt.%, respectively. These weight losses were attributed to physical adsorbed water on the surfaces of the tested TiO₂/CNT hybrids samples. It was noted that no other exothermic peak corresponded to residing carbon species in the DSC plots below 470 °C, further confirming only the carbonaceous material formed from the heat treating of CNT remained in TiO₂/CNT hybrids. Therefore, the chemical compositions of TiO₂/CNTs-60 C and the TiO₂/CNTs-110 C were approximately 63.85 wt.% TiO₂ anatase and 36.15 wt.% CNTs (except 4 wt.% physical adsorbed water), 72.42 wt.% TiO₂ anatase and 27.58 wt.% CNTs (except 5 wt.% physical adsorbed water), respectively. Therefore, increasing the initial reaction temperature benefited the TiO₂ deposition on the CNT surfaces. As we know, small TiO₂ aggregates can easily be lost during centrifugation. The higher TiO₂ nanoparticle content of the TiO₂/CNTs-110 C sample suggested that the TiO₂ nanoparticles were better distributed and covered the 3D TiO₂/CNTs hybrid network more fully (Figs. 2a and 3a), as was consistent with the FE-SEM observations. The effects of the initial reaction temperature and the subsequent thermal treatment on the properties of TiO₂/CNT hybrids were further studied using Raman data. As shown in Fig. 5, Raman peaks at approximately 152, 389, 516 and 622 cm⁻¹ were observed for both the TiO₂/CNTs-60 C and TiO₂/CNTs-110 C samples, which could be indexed as the E_g, B_{1g}, A_{1g}/B_{1g}, and E_g modes of a typical anatase TiO₂ phase, respectively [27]. The E_g mode of bare TiO₂ was located at 146 cm⁻¹ (inset in Fig. 5) [22,28]. The dependence of blue shifts of the Raman peaks from the crystal dimension might have various explanations. A blue shift was sometimes attributed to a non-stoichiometry caused by oxygen vacancies in the bulk of TiO₂ [29]. However, in our case, the thermal treatment was performed in air and the nonstoichiometry was expected to be negligible. There were two other possible reasons: a phonon confinement effect and the strain applied by the surface interaction, which might be responsible for the Raman shift. Bersani et al. observed a comparable blue shift (from 144 cm⁻¹ to 149 cm⁻¹) and associated it with phonon confinement caused by a decrease in crystal size of anatase from 50 nm to 5 nm [30]. In this work, the particle size of the TiO₂/

CNTs-110 C sample (~8–10 nm) in Fig. 3c and d was larger than that of the bare TiO₂ sample (~2–3 nm). A blue shift (from 146 cm⁻¹ to 152 cm⁻¹) and broadening of the Raman peak for the TiO₂/CNTs-110 C sample with the larger grain size were observed, thus suggesting that this blue shift and broadening might not be as a result of phonon confinement (the broadening of Raman peak accompanied by the decrease of grain size) but an additional contribution. It has been reported that the surface strain affects the surface structure of nanoparticles and results in the shifts and the broadening of Raman peaks of the nanoparticles [31]. Therefore, the blue-shifted E_g of the TiO₂/CNTs-110 C sample might result from the interaction between the TiO₂ and CNTs. Similar blue shift (from 144 cm⁻¹ to 153 cm⁻¹) was also reported between TiO₂ and graphene [27]. Presumably, a similar effect occurred between TiO₂ and CNTs. These interactions were very important for creating a strong connection between the TiO₂ and CNTs. Two broad peaks at approximately 1345 and 1570 cm⁻¹ were observed in the Raman spectra of the TiO₂/CNTs-60 C hybrids, the TiO₂/CNTs-110 C hybrids and CNTs (PEO); these peaks were assigned to the D (breathing mode of k-point phonons of A_{1g} symmetry usually attributed to local defects and disorders) and G peaks (attributed to the E_{2g} phonon of C sp² atoms) of the CNTs [8]. Additionally, the D peak of CNTs in the TiO₂/CNTs-110 C sample also shifted to higher wave-number (1–2 cm⁻¹ blue shift) and no shift of the G peak was observed comparing to that of the CNT (PEO) sample, as comparing to pure dodecylbenzenesulfonic acid (DBS) no shift of the Raman peak at 1596 cm⁻¹ corresponding to the C–C stretching in DBS/TiO₂ nanoparticles occurred [32]. The I_D/I_G peak intensity ratio revealed the carbon's degree of graphitization, which was 0.908, 0.806, 0.745 and 0.961, corresponding to the TiO₂/CNTs-60 C hybrids, the TiO₂/CNTs-110 C hybrids, pristine CNTs and CNTs (PEO), respectively. Therefore, the I_D/I_G ratios of the CNTs (PEO) and CNTs were the largest and the smallest, respectively. However, when the initial reaction temperature increased, the I_D/I_G ratio decreased. The smaller I_D/I_G value suggested that fewer defects and less disorder occurred in the graphitized structures. We assumed that the I_D/I_G value depended on the degree of oxidation formed on the CNT surfaces during the thermal treatment in air for PEO removal calcination. Coverage level of TiO₂ nanoparticles on the CNTs surfaces, namely, exposure degree of the CNTs surfaces in air, affected the oxidation degrees of the CNTs surfaces during the thermal treatment. Compared to the TiO₂/CNTs-60 C sample (0.908), the TiO₂/CNTs-110 C sample had a lower I_D/I_G value (0.806); therefore, it had a more ordered structure and more C sp² atoms in the CNTs within the hybrids. The lowered exposure of the CNT surfaces in air (specifically, better TiO₂ nanoparticle coverage in the 3D TiO₂/CNT hybrid network) for the TiO₂/CNTs-110 C sample may explain this result. The amount of C sp² atoms in the CNTs of the hybrid materials dictated the electronic conductivity. Therefore, the TiO₂/CNTs-110 C sample should be more electronically conductive than the TiO₂/CNTs-60 C sample, leading to a faster electron transfer for lithium ion batteries. The TiO₂/CNTs-110 C sample's electronic conductivity was 5.13 S cm⁻¹, confirming the formation of CNT conductive networks in the hybrid materials.

The interaction between the TiO₂ and CNTs was further investigated using XPS. Fig. 6a presents the Ti, O, and C elements with their chemical binding energies: Ti(2p_{3/2}) (458.9 eV), Ti(2p_{1/2}) (464.56 eV), O(1s) (530.1 eV) and C(1s) (284 eV). The atomic ratio of C, O and Ti was 72.3: 20.4: 7.3. The O/Ti ratio was 2.8 (>2 of the stoichiometry of titania) due to the oxidation of the CNT surfaces in air. Deconvolution of the C(1s) peak in the XPS spectrum in Fig. 6b revealed three types of carbon bonds: C–C, C=C or C–H (283.9 eV), C–O (284.5 eV), and O–C–O (285.4 eV). The Ti(2p) spectrum (Fig. 6c) displayed the spin orbit split lines for Ti(2p_{3/2}) and Ti(2p_{1/2}) at 458.9 and 464.56 eV, respectively; these signals were

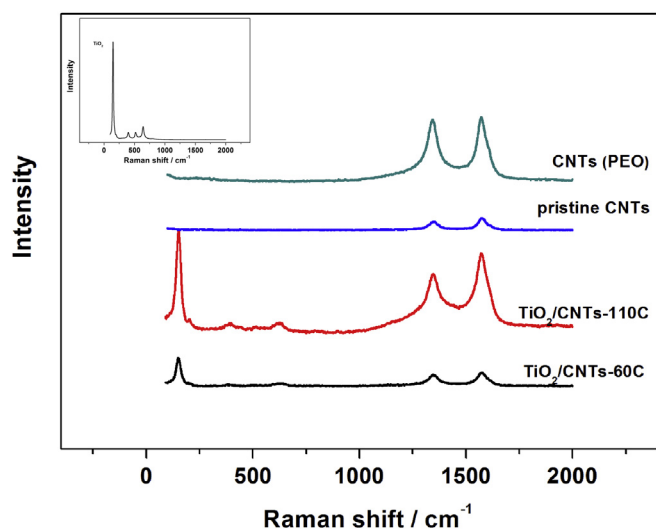


Fig. 5. Raman spectra of the TiO₂ (inset), CNTs (PEO), pristine CNTs, TiO₂/CNTs-110 C and TiO₂/CNTs-60 C samples.

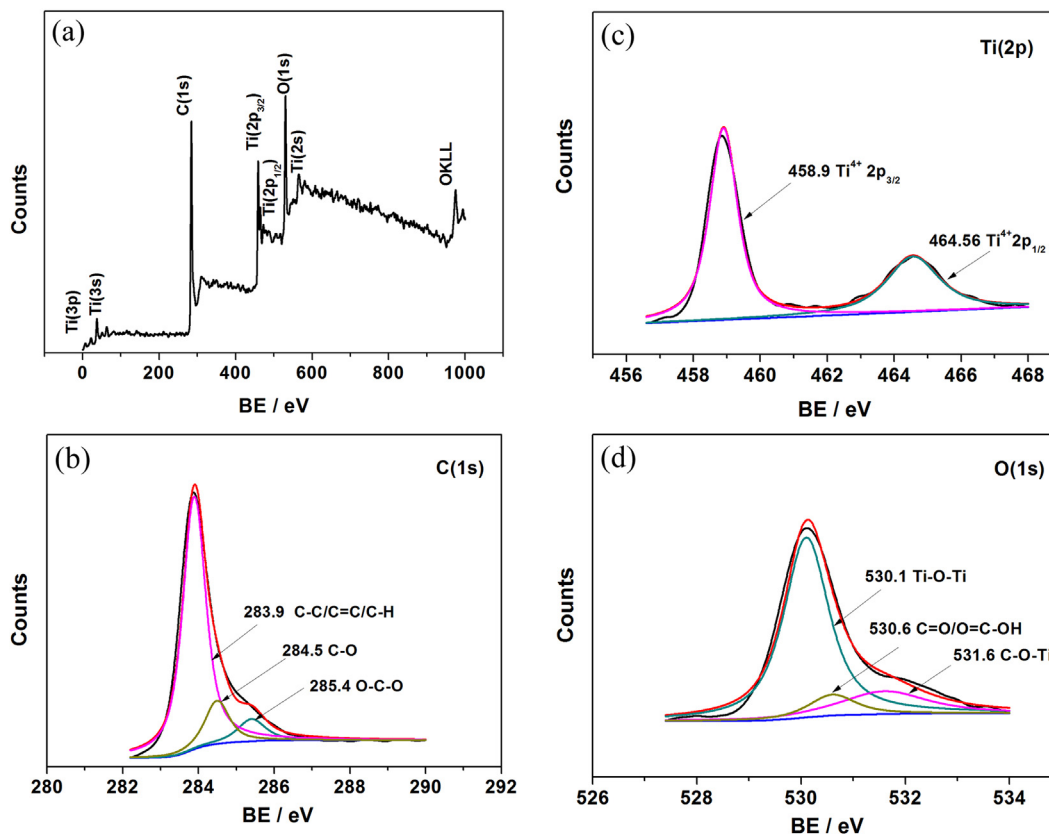


Fig. 6. X-ray photoelectron spectrum for the $\text{TiO}_2/\text{CNTs-110 C}$ surface: (a) survey spectrum showing C(1s), Ti(2s), Ti(2p), Ti(3s), Ti(3p) and O(1s); (b) deconvoluted C(1s) region of XP spectrum; (c) the Ti(2p) binding energy region showing spin orbit splitting of $2p_{3/2}$ and $2p_{1/2}$; (d) deconvoluted O(1s) of XP spectrum region.

characteristic for the Ti^{4+} oxidation state. The corresponding O(1s) spectrum in Fig. 6d was broad and asymmetric; it could be deconvoluted into three peaks, indicating that three different oxygen species existed. A peak with a 530.1 eV binding energy was assigned to the Ti–O–Ti of TiO_2 . The peaks at 530.6 and 531.6 eV were attributed to the C=O or O=C–OH and Ti–O–C bonds, respectively [8]. As we know, under oxygen-poor conditions, substitutional (to oxygen) carbon and oxygen vacancies are favored, whereas, under oxygen-rich conditions, interstitial and substitutional (to Ti) C atoms are preferred [33]. In our case, the thermal treatment was performed in air, and thus Ti–O–C bonds were preferred, not Ti–C bonds, supported by the O(1s) spectrum. The Ti–O–C bond formation not only accelerated the electron transfer but also stabilized the hybrid's structure during the charge/discharge process.

The pore structures of the 3D TiO_2/CNTs conductive network hybrids were investigated in detail using nitrogen isothermal adsorption. For comparison, bulk TiO_2 and pristine CNTs were studied. As summarized in Table 1, the Brunauer–Emmett–Teller (BET) specific surface area and pore volume of the TiO_2 obviously increased after incorporating the CNTs from 108.8 to 122.4 $\text{m}^2 \text{g}^{-1}$ and 0.246–0.603 $\text{cm}^3 \text{g}^{-1}$, respectively, which was because that PEO on the CNTs surface in the reaction process changed the TiO_2

nucleation and improved TiO_2 particle dispersion in the TiO_2/CNTs hybrids, forming a highly open porous structure. As shown in Fig. 7, the $\text{TiO}_2/\text{CNTs-110 C}$, TiO_2 and pristine CNT samples exhibited type-IV isotherm curves with a hysteresis loop, revealing their mesoporosity. According to the Barrett–Joyner–Halenda (BJH) pore size distribution (inset in Fig. 7a), the $\text{TiO}_2/\text{CNTs-110 C}$ sample contained four pore types that averaged 3.3, 8.1, 21.3 and 44.1 nm in diameter. The 8.1 nm pores resulted from the TiO_2 nanoparticles, while the 3.3 nm pores were attributed to CNTs, as confirmed by BJH results for the CNTs (inset in Fig. 7c). The large pores (10–100 nm) were interspersed pores among the nanotubes, as indicated by in the $\text{TiO}_2/\text{CNTs-110 C}$ and pristine CNTs samples (insets in Fig. 7a and c). The major pore size attributed to the TiO_2 nanoparticles in the $\text{TiO}_2/\text{CNTs-110 C}$ hybrids (8.1 nm) was larger than that for the bare TiO_2 nanoparticles (4.8 nm) (inset in Fig. 7b).

3.2. Electrode performance

The electrochemical performance of the materials during lithium insertion/extraction was first investigated using galvanostatic charge–discharge curves at different rates. As indicated by Fig. S4 for the $\text{TiO}_2/\text{CNTs-60 C}$ electrodes, the initial discharge capacities (165, 147, 118, 86 and 64 mA h g^{-1}) were achieved at current densities of 100, 500, 1000, 2000 and 4000 mA g^{-1} , respectively (1 C = 168 mA g^{-1}); the capacities were 157, 118, 97, 75 and 59 mA h g^{-1} after 100 cycles at the corresponding rates. Because the Li storage in CNTs occurred mainly below 1.0 V [14], the capacity contributed by the TiO_2/CNTs hybrids anodes between 1.0 and 3.0 V was attributed to the TiO_2 anatase phase (the capacity of the hybrids was calculated based on the whole mass). A significant increase in the discharging capacity, especially at

Table 1
Parameters associated with the porous structure of the samples.

Sample	BET surface area [$\text{m}^2 \text{g}^{-1}$]	Pore volume [$\text{cm}^3 \text{g}^{-1}$]
TiO_2	108.76	0.2458
Pristine CNTs	113.97	0.6159
$\text{TiO}_2/\text{CNTs-110 C}$	122.42	0.6031

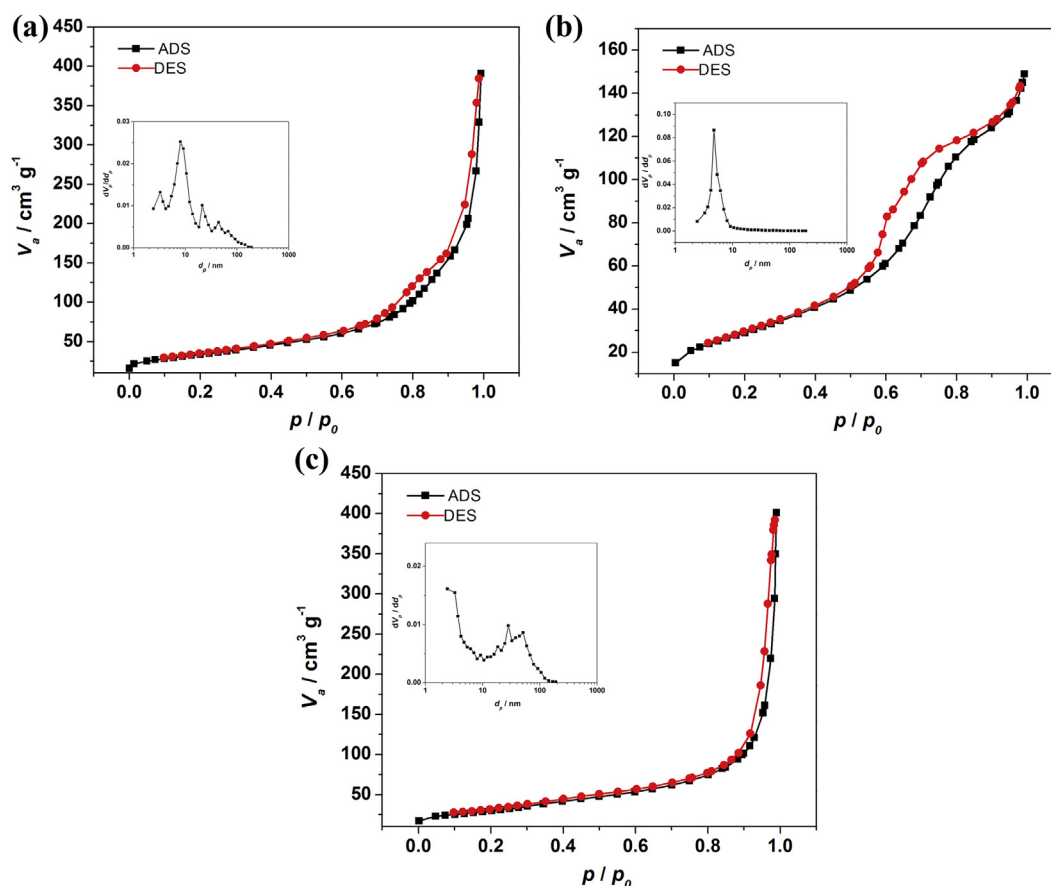


Fig. 7. N_2 adsorption–desorption isotherms of $\text{TiO}_2/\text{CNTs-110 C}$ (a), TiO_2 (b) and pristine CNTs (c), the insets showing BJH pore-size distributions of these samples.

high discharge rates, was observed for the $\text{TiO}_2/\text{CNTs-110 C}$ electrodes relative to the $\text{TiO}_2/\text{CNTs-60 C}$ electrodes. As shown in Fig. 8, the initial discharge capacities reached 220, 158, 140, 125 and 103 mA h g^{-1} at rates of 100, 500, 1000, 2000 and 4000 mA g^{-1} , respectively, for the $\text{TiO}_2/\text{CNTs-110 C}$ electrodes, while the capacities were 203, 148, 139, 116 and 101 mA h g^{-1} over 100 cycles at the corresponding rates; the Coulombic efficiencies exceeded 98%. This improvement might be explained by the higher coverage of uniformly distributed anatase TiO_2 particles across the mesoporous TiO_2/CNT 3D conductive network in $\text{TiO}_2/\text{CNTs-110 C}$, as confirmed by the TEM and TGA results. The rate capacities of the $\text{TiO}_2/\text{CNTs-110 C}$ electrodes were comparable to some of the best results reported in the literature for materials using graphene [3,27] or carbon nanohorns [9]. Notably, at extremely high rates (8000 mA g^{-1} (47.6 C) and 15000 mA g^{-1} (89 C)), the initial discharging capacity of the $\text{TiO}_2/\text{CNTs-110 C}$ electrode reached 91 and 79 mA h g^{-1} , respectively, and there was almost no decay in capacity after 100 cycles, suggesting that the $\text{TiO}_2/\text{CNTs-110 C}$ electrode had excellent cycling stability.

To evaluate the cyclability of the $\text{TiO}_2/\text{CNTs-110 C}$ anodes for LIBs, additional galvanostatic discharge/charge measurements at a higher rate (15000 mA g^{-1}) were conducted with a single cell. Fig. 9 illustrates the continuous cycling results for 900 cycles at 15000 mA g^{-1} . The initial discharge capacity for the $\text{TiO}_2/\text{CNTs-110 C}$ anodes reached 79 mA h g^{-1} , while the capacity decreased to 71 mA h g^{-1} during the first 50 cycles; this value was retained for the remaining 850 cycles. Remarkable capacity retention was observed: approximately 90% (71 mA h g^{-1}) of the initial discharge capacity was retained after 900 cycles at

15000 mA g^{-1} , and the Coulombic efficiency reached nearly 100% during each cycle, indicating excellent long term cycling stability. To illustrate the importance of the 3D conductive network for the electrochemical properties of the $\text{TiO}_2/\text{CNTs-110 C}$ anodes, cyclic voltammograms of the $\text{TiO}_2/\text{CNTs-110 C}$ and mesoporous TiO_2 electrodes over 1.0–3.0 V at 0.1, 0.5, 1, 2 and 4 mV s^{-1} were evaluated and compared. As shown in Fig. 10, a pair of redox peaks at 1.70 and 1.97 V appeared in the cyclic voltammograms

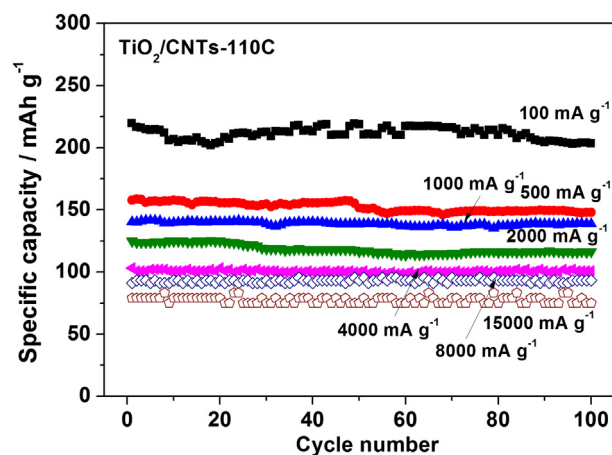


Fig. 8. Cycling performance of the $\text{TiO}_2/\text{CNTs-110 C}$ electrodes with 100 cycles between 1.0 and 3.0 V at the current densities of 100, 500, 1000, 2000, 4000, 8000 and 15000 mA g^{-1} , respectively.

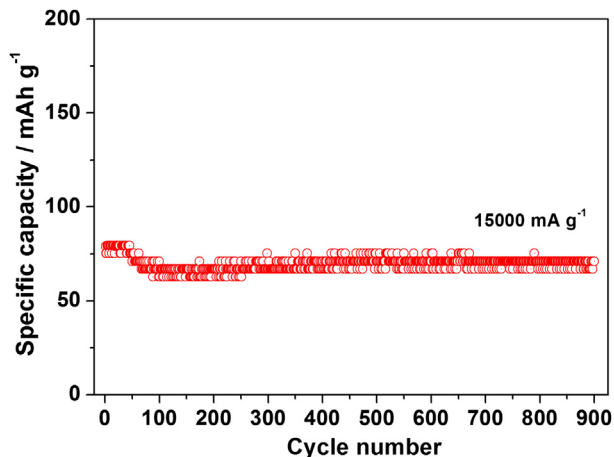


Fig. 9. Long term cycling performances of the $\text{TiO}_2/\text{CNTs-110 C}$ electrodes at a superior high rate of 15000 mA g^{-1} for 900 cycles (voltage range: 1.0–3.0 V).

of both the $\text{TiO}_2/\text{CNTs-110 C}$ and mesoporous TiO_2 electrodes at 0.1 mV s^{-1} . The peaks at approximately 1.7 V (insertion process) and 2.0 V (extraction process) were related to the phase transition between the tetragonal and orthorhombic phases for the Li intercalation into anatase TiO_2 [23]; this result re-confirmed the formation of the anatase TiO_2 phase in the $\text{TiO}_2/\text{CNTs-110 C}$ and mesoporous TiO_2 samples. The $\text{TiO}_2/\text{CNTs-110 C}$ anodes demonstrated larger redox currents than the mesoporous TiO_2 composed of 2–3 nm anatase particles. The peak separation increased between the anodic and cathodic peaks as the scan rate increased for both the $\text{TiO}_2/\text{CNTs-110 C}$ (from 0.27 to 0.81 V) and mesoporous TiO_2 (from 0.27 to 0.73 V) electrodes, indicating that the polarization increased when the charging–discharging rate increased. Compared to the mesoporous TiO_2 (2–3 nm anatase particles), $\text{TiO}_2/\text{CNTs-110 C}$ presented larger peak separation because its particles were larger (8–10 nm). However, the $\text{TiO}_2/\text{CNTs-110 C}$ electrode exhibited a larger initial discharging capacity at all charge–discharge rates relative to the mesoporous TiO_2 anodes, as indicated by Fig. 11a and b. According to Fig. 11d, the initial specific capacity for the mesoporous TiO_2 anodes reached as low as 92 mA h g^{-1} at 100 mA g^{-1} , and the reversible capacity decreased during the initial 20 cycles and stabilized during the subsequent cycles (33 mA h g^{-1}). The discharge capacity at 500–4000 mA g^{-1} was less than 30 mA h g^{-1} and further decreased, reaching nearly zero when the current density increased above 4000 mA g^{-1} . Therefore, mesoporous TiO_2 anodes exhibited poorer rate performances and cycling stability relative to the $\text{TiO}_2/\text{CNTs-110 C}$ anodes in Fig. 8 because they lacked the efficient electron-conducting paths. Therefore, the 3D conductive networks in the hybrids were indispensable to achieve a high charging–discharge rate.

Electrochemical impedance spectroscopy measurements of the $\text{TiO}_2/\text{CNTs-110 C}$ and mesoporous TiO_2 anodes activated by two cycles at the open circuit voltage ($\sim 1.7 \text{ V}$) were performed to understand the improved high-rate performance; the typical results are presented in Fig. 11c. The impedance spectra can be fitted based on a reasonable equivalent circuit in accordance with the physical mechanism of the Li-ion insertion/extraction for the electrodes (Fig. 11c inset): R_Ω represented the uncompensated bulk resistance of the electrolyte, separator and electrode; the (C_1R_1) parallel element corresponded to the material conductivity, electrode roughness and inhomogeneous reaction at the surface; and the $(Q(R_{ct}W))$ element related to the electronic and ionic resistance between the electrode and electrolyte, as well as the Warburg

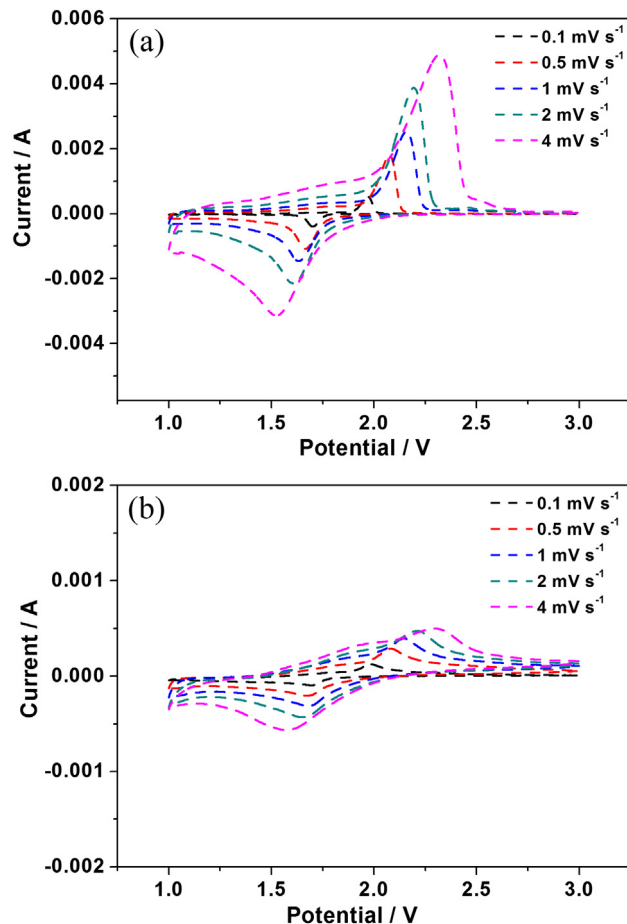


Fig. 10. Cyclic voltammograms of the $\text{TiO}_2/\text{CNTs-110 C}$ (a) and mesoporous TiO_2 (b) electrodes in the voltage range of 1.0–3.0 V at the scan rates of 0.1, 0.5, 1, 2 and 4 mV s^{-1} , respectively.

resistance associated with diffusion [11]. The expression for the admittance response of the constant phase element CPE (Q) was as follows [34]:

$$Y = Y_0 \omega^n \cos\left(\frac{n\pi}{2}\right) + jY_0 \omega^n \sin\left(\frac{n\pi}{2}\right) \quad (1)$$

where ω was the angular frequency and j was the imaginary unit. The CPE was a resistor when $n = 0$, a capacitor with capacitance of C when $n = 1$, an inductor when $n = -1$, and a Warburg resistance when $n = 0.5$. σ was the Warburg factor satisfying well with the following equation:

$$\sigma = \frac{1}{\sqrt{2}Y_0} \quad (2)$$

Based on this equivalent circuit model, the electrochemical parameters for fitting were obtained; they are listed in Table 2. Compared to that of the mesoporous TiO_2 anode, both R_Ω and R_1 decreased for the $\text{TiO}_2/\text{CNTs-110 C}$ anode; this result was mainly attributed to the higher electronic conductivity of the hybrids. Notably, a large decrease in the charge-transfer resistance from 131.7 to 29.85Ω occurred, corresponding to mesoporous TiO_2 and $\text{TiO}_2/\text{CNTs-110 C}$ anodes, respectively; therefore, the electrode/electrolyte interface was greatly improved during the Li ions' insertion and extraction. The lithium-ion diffusion coefficient may be estimated using the inclined lines in the Warburg region and the following equation [34]

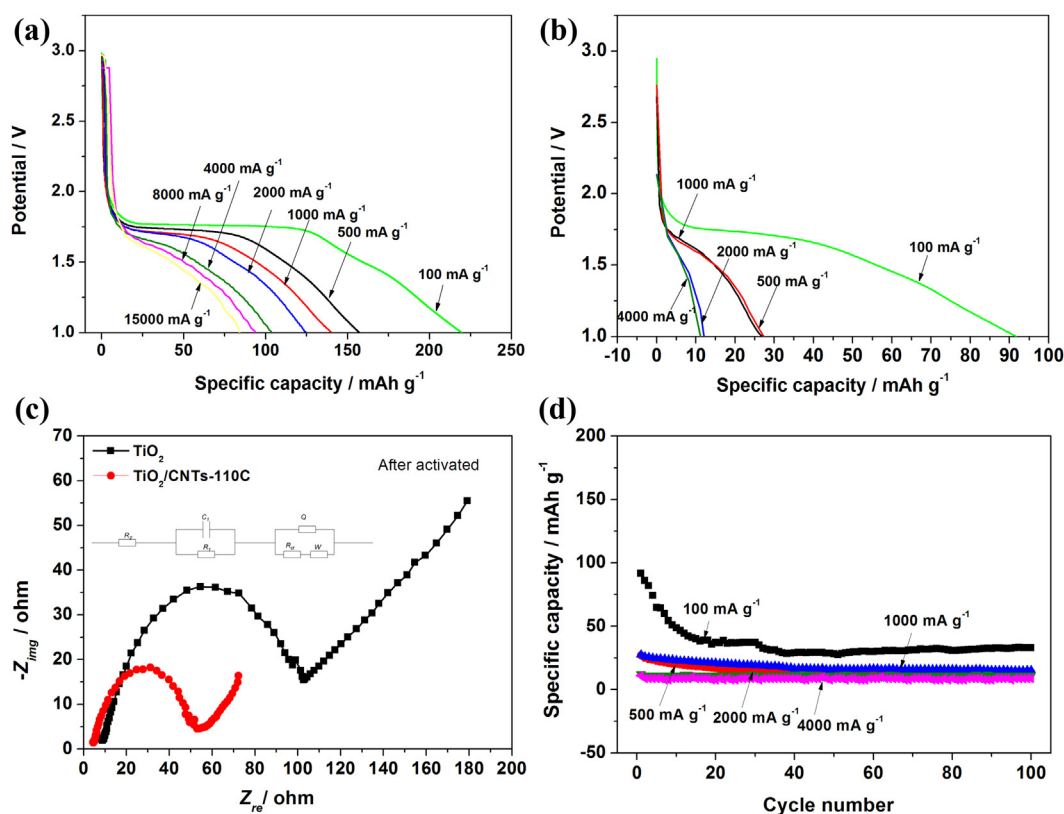


Fig. 11. Initial discharge profiles of the TiO₂/CNTs-110 C (a) and mesoporous TiO₂ (b) electrodes at current densities of 100, 500, 1000, 2000 and 4000 mA g⁻¹; (c) electrochemical impedance spectra of the TiO₂/CNTs-110 C and mesoporous TiO₂ electrodes at open circuit voltage (~1.70 V); (d) cycling performances of mesoporous TiO₂ electrodes at current densities of 100, 500, 1000, 2000 and 4000 mA g⁻¹ (voltage range: 1.0–3.0 V).

$$D_{\text{Li}} = \frac{R^2 T^2}{2A^2 n^4 F^4 C^2 \sigma^2} \quad (3)$$

where R was the gas constant, T was the absolute temperature, A was the surface area of the cathode, n was the number of electrons per molecule during reaction, F was the Faraday constant, C was the concentration of lithium ions ($7.69 \times 10^{-3} \text{ mol cm}^{-3}$), and σ was the Warburg factor (Eq. (2)) based on the fitting value ($W - Y_0$). The lithium ions' diffusion coefficients in the TiO₂/CNTs-110 C and mesoporous TiO₂ anodes were calculated using Eq. (3): 1.4163×10^{-12} and $2.5912 \times 10^{-14} \text{ cm}^2 \text{ s}^{-1}$, respectively. Therefore, the lithium ions' diffusion was dramatically increased in the hybrid anode. The TiO₂/CNTs-110 C anode's greatly improved charge transfer process meant that it was more capable of facilitating lithium ion transfer at a high charge/discharge rate.

The superior high rate performances and excellent long-term cyclability observed for the TiO₂/CNTs-110 C anodes were attributed to their unique mesoporous TiO₂/CNT 3D conductive network structure. This structure generated three benefits: (1) the chain structure features greatly reduced particle reunion chance and the contact resistance between adjacent particles, fully improving high power characteristics of the electrode materials and nanostructure

could further improve the electrochemical activity; (2) self-assembled 3D chain network structures with rich, overlapping mesopores and/or macropores greatly shortened the lithium ion diffusion path, ensuring that electrolyte can quickly contact with the active electrode material surface and was enough to maintain electrolyte at high charge/discharge rates, and accelerating the lithium ion transport joining with the increased lithium diffusion coefficient to improve rate performances; (3) this 3D CNT

Table 2

The fitted impedance parameters of the equivalent circuit in Fig. 11c.

Sample	R_{ct} / ohm	C_1/F	R_1/ohm	$Q - n$	$Q - Y_0/S \text{ s}^{1/2}$	R_{ct}/ohm	$W - Y_0/S \text{ s}^{1/2}$
TiO ₂	5.616	1.131E-5	59.93	0.319	0.004926	131.7	0.007158
TiO ₂ /CNTs-110 C	2.908	1.257E-5	29.7	0.388	0.003517	29.85	0.05292

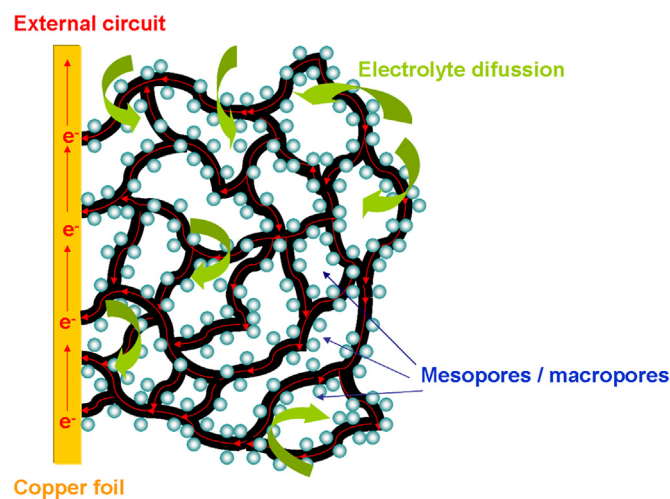


Fig. 12. Schematic model for the charge high-rate process, showing the facilitated electron transport through 3D CNTs conductive network and electrolyte diffusion through mesopores and/or macropores.

conductive network contains Ti–O–C bonds that could promote fast electron transfer and reduce the volume expansion to stabilize the material's structure during lithium ion insertion and extraction.

A schematic model for the charge process at high rates is proposed in Fig. 12. During the high-rate charge process, the ionic charges moved quickly toward the TiO₂ nanoparticles' surfaces through the electrolyte, which was because that they could obtain timely supplementary due to the presence of mesopores and/or macropores in the hybrid structure. To maintain the TiO₂ particles' electrical neutrality, electrons passed through the 3D CNTs conductive network before being collected by the copper foil and then passed along the external circuit to return. The high-rate discharge process was the reverse.

4. Conclusions

Mesoporous TiO₂/CNTs 3D conductive network hybrid nanostructures were synthesized using a facile PEO-aided self-assembled process. The PEO was utilized to functionalize and stabilize the 3D conductive CNT network through non-covalent interactions. While being mediated by PEO on the sidewalls of 3D conductive CNT network, uniform anatase TiO₂ nanoparticles were generated in situ and deposited onto the CNTs/PEO hybrids. The anatase TiO₂ nanoparticles' coverage of the CNT surfaces could be controlled by modulating the amounts of the precursors and the initial reaction temperature. This synthetic strategy is relatively simple and may be scaled-up for practical applications. Mesoporous TiO₂/CNT 3D conductive network hybrid anodes with high electronic conductivity (5.13 S cm⁻¹) for lithium-ion batteries exhibit a large specific capacity, a superior high rate capability, and excellent long term cyclability. These characteristics were attributed to the material's high rate of ionic/electronic conduction and excellent structural stability; these parameters arose from the material's rich, overlapping mesopores and/or macropores, 3D CNT conductive network and Ti–O–C bonds. Utilizing 3D CNT conductive network electrodes with continuous conductive paths is a promising method for developing electrodes with high-rate and long term cycling performance for lithium ion batteries. This high-rate mesoporous TiO₂/CNT anode material holds great potential for applications in power type lithium ion batteries of EVs and HEVs.

Acknowledgments

This work was partially supported by the “National Science Foundation for Distinguished Young Scholars of China” under contract No. 51025209, by “National Nature Science Foundation of China” under contract No. 21103089 and by “Key Projects in Nature Science Foundation of Jiangsu Province” under contract No.

BK2011030, Prof. Shao also acknowledges the ARC future fellowship.

Appendix A. Supplementary data

Supplementary data related to this article can be found at <http://dx.doi.org/10.1016/j.jpowsour.2013.12.090>.

References

- [1] J.M. Tarascon, M. Armand, *Nature* 414 (2001) 359–367.
- [2] J. Maier, *Nat. Mater.* 4 (2005) 805–815.
- [3] D. Wang, D. Choi, J. Li, Z. Yang, Z. Nie, R. Kou, D. Hu, C. Wang, L.V. Saraf, J. Zhang, I.A. Aksay, J. Liu, *ACS Nano* 3 (2009) 907–914.
- [4] S.H. Nam, H.-S. Shim, Y.-S. Kim, M.A. Dar, J.G. Kim, W.B. Kim, *ACS Appl. Mater. Interfaces* 2 (2010) 2046–2052.
- [5] M. Mancini, P. Kubiak, M. Wohlfahrt-Mehrens, R. Marassi, *J. Electrochem. Soc.* 157 (2010) A164.
- [6] Y.G. Guo, Y.S. Hu, W. Sigle, J. Maier, *Adv. Mater.* 19 (2007) 2087–2091.
- [7] P.S. Herle, B. Ellis, N. Coombs, L.F. Nazar, *Nat. Mater.* 3 (2004) 147–152.
- [8] J. Wang, Y. Zhou, B. Xiong, Y. Zhao, X. Huang, Z. Shao, *Electrochim. Acta* 88 (2013) 847–857.
- [9] W. Xu, Z. Wang, Z. Guo, Y. Liu, N. Zhou, B. Niu, Z. Shi, H. Zhang, *J. Power Sources* 232 (2013) 193–198.
- [10] G.R. Goward, F. Leroux, L.F. Nazar, *Electrochim. Acta* 43 (1998) 1307–1313.
- [11] Y. Zhou, J. Wang, Y. Hu, R. O'Hayre, Z. Shao, *Chem. Commun.* 46 (2010) 7151–7153.
- [12] C.K. Chan, X.F. Zhang, Y. Cui, *Nano Lett.* 8 (2008) 307–309.
- [13] G.F. Ortiz, I. Hanzu, T. Djenizian, P. Lavela, J.L. Tirado, P. Knauth, *Chem. Mater.* 21 (2009) 63–67.
- [14] F.-F. Cao, Y.-G. Guo, S.-F. Zheng, X.-L. Wu, L.-Y. Jiang, R.-R. Bi, L.-J. Wan, J. Maier, *Chem. Mater.* 22 (2010) 1908–1914.
- [15] S.-W. Kim, T.H. Han, J. Kim, H. Gwon, H.-S. Moon, S.-W. Kang, S.O. Kim, K. Kang, *ACS Nano* 3 (2009) 1085–1090.
- [16] J. Wang, Y. Zhou, Z. Shao, *Electrochim. Acta* 97 (2013) 386–392.
- [17] Y. Sun, Q. Wu, G. Shi, *Energy Environ. Sci.* 4 (2011) 1113.
- [18] W.-D. Zhang, B. Xu, L.-C. Jiang, *J. Mater. Chem.* 20 (2010) 6383–6391.
- [19] E.A. Whittitt, A.R. Barron, *Nano Lett.* 3 (2003) 775–778.
- [20] J. Wang, Y. Zhou, Y. Hu, R. O'Hayre, Z. Shao, *J. Phys. Chem. C* 115 (2011) 2529–2536.
- [21] D. Tasis, N. Tagmatarchis, A. Bianco, M. Prato, *Chem. Rev.* 106 (2006) 1105–1136.
- [22] D. Eder, A.H. Windle, *Adv. Mater.* 20 (2008) 1787–1793.
- [23] I. Moriguchi, R. Hidaka, H. Yamada, T. Kudo, H. Murakami, N. Nakashima, *Adv. Mater.* 18 (2006) 69–73.
- [24] H. Zhou, L. Liu, X. Wang, F. Liang, S. Bao, D. Lv, Y. Tang, D. Jia, *J. Mater. Chem. A* 1 (2013) 8525.
- [25] S. Ding, J.S. Chen, X.W. David Lou, *Adv. Funct. Mater.* 21 (2011) 4120–4125.
- [26] P. Zhu, Y. Wu, M.V. Reddy, A. Sreekumaran Nair, B.V.R. Chowdari, S. Ramakrishna, *RSC Adv.* 2 (2012) 531–537.
- [27] L. Shen, X. Zhang, H. Li, C. Yuan, G. Cao, *J. Phys. Chem. Lett.* 2 (2011) 3096–3101.
- [28] X. Gao, H. Zhu, G. Pan, S. Ye, Y. Lan, F. Wu, D. Song, *J. Phys. Chem. B* 108 (2004) 2868–2872.
- [29] J.C. Parker, R.W. Siegel, *J. Mater. Res.* 5 (1990) 1246–1252.
- [30] D. Bersani, P.P. Lottici, X.-Z. Ding, *Appl. Phys. Lett.* 72 (1998) 73–75.
- [31] B.C. Gou, Z.X. Liu, Q.L. Cui, H.B. Yang, Y.N. Zhao, G.T. Zou, *High. Press. Res.* 1 (1989) 185–191.
- [32] C.Y. Xu, P.X. Zhang, L. Yan, *J. Raman Spectrosc.* 32 (2001) 862–865.
- [33] C. Di Valentini, G. Pacchioni, A. Selloni, *Chem. Mater.* 17 (2005) 6656–6665.
- [34] A.J. Bard, L.R. Faulkner, *Electrochemical Methods*, second ed., Wiley, 2001.